Article:
Efthymiadis, P., Pinna, C. orcid.org/0000-0002-9079-1381 and Yates, J.R. (2019) Fatigue crack initiation in AA2024: a coupled micromechanical testing and crystal plasticity study. Fatigue and Fracture of Engineering Materials and Structures, 42 (1). pp. 321-338. ISSN 8756-758X

https://doi.org/10.1111/ffe.12909

Received: 9 June 2018 | Revised: 23 July 2018 | Accepted: 25 July 2018

DOI: 10.1111/ffe.12909

ORIGINAL CONTRIBUTION

WILEY

Fatigue crack initiation in AA2024: A coupled micromechanical testing and crystal plasticity study

Panos Efthymiadis[1,2] | Christophe Pinna[2] | John R. Yates[3]

[1] GKN Aerospace, Global Technologies, Golf Course Lane, Bristol BS34 9AU, UK

[2] Department of Mechanical Engineering, The University of Sheffield, Sheffield S1 3JD, UK

[3] Simuline Ltd., Derbyshire S18 1QD, UK

Correspondence
Panos Efthymiadis, GKN Aerospace, Global Technologies, Golf Course Lane, Filton, Bristol BS34 9AU, UK.
Email: panos.efthymiadis@gknaerospace.com

Funding information
Engineering and Physical Sciences Research Council, Grant/Award Number: EP/F023464/1

Abstract

A new combined experimental and modelling approach has been developed in order to understand the physical mechanisms that lead to crack nucleation in a polycrystalline aluminium alloy AA2024 undergoing cyclic loading. Four-point bending low-cycle fatigue tests were performed inside the chamber of a scanning electron microscope on specimens with a through-thickness central hole, introduced to localize stresses and strains in a small region on the top surface of the sample. Fatigue crack initiation and small crack growth mechanisms were analyzed through high-resolution scanning electron microscope images, local orientation measurements using electron-back-scattered-diffraction, and local strain measurements using digital image correlation. A crystal plasticity finite element model was developed to simulate the cyclic deformation behaviour of AA2024. Two-dimensional Voronoi-based microstructures were generated, and the material parameters for the constitutive equations (including both isotropic and kinematic hardening) were identified using monotonic and fully reversed cyclic tests. A commonly used fatigue crack initiation criterion found in the literature, the maximum accumulated plastic slip, was evaluated in the crystal plasticity finite element model but could not predict the formation of cracks away from the edge of the hole in the deformed specimens. A new criterion combining 2 parameters: The maximum accumulated slip over each individual (critical) slip system and the maximum accumulated slip over all slip systems were formulated to reproduce the experimental locations of crack nucleation in the microstructure.

1 | INTRODUCTION

Even though the fatigue of metals has been studied for more than 2 centuries,[1] much research is still needed to understand and predict the conditions leading to crack formation in polycrystalline microstructures under cyclic loading. Fatigue crack initiation (FCI) and small crack growth (SCG) are the 2 phases of crack development that are most influenced by the microstructure.[2] As a result, significant scatter is commonly observed in experimental results,[3] leading to high uncertainty in fatigue model prediction. Microstructure-informed models therefore need to be developed to improve the reliability of fatigue life calculations for engineering components.[4,5] Recent modelling studies on FCI

and SCG have covered a range of polycrystalline metals, such as aluminium alloys,[6-8] titanium,[9-11] stainless steels,[12] and nickel-based superalloys.[10,13-15]

The physical mechanisms that lead to FCI are highly localized. For instance, dislocation dipoles, interface decohesion, triple points, and second-phase particles can lead to strain localization followed by crack nucleation.[1,3,5,10] The propagation of a short crack depends on the resistance and strength of the matrix. Depending on the location of the crack, whether it is close or not to a grain boundary (GB), crack acceleration or deceleration can also occur.[16] Particles embedded in the matrix may facilitate further propagation if the particles break in a brittle manner or retard crack growth if the particles break in a ductile manner. As a result, factors affecting localized damage nucleation and SCG can be very complex. A reliable physically based FCI criterion must therefore capture the effect of various likely mechanisms leading to the formation of a fatigue crack at the scale of the microstructure. Various computational approaches, such as crystal plasticity finite element (CPFE) modelling, molecular dynamics, discrete dislocation dynamics, and conventional continuum-based finite element modelling, have been utilized with different criteria to model FCI in various studies.[3-8,10,15,17,18] Crystal plasticity finite element modelling simulations have been shown to model FCI accurately and efficiently.[5] However various crystal plasticity-based criteria have been proposed in the literature. Cheong et al[18] used an energy based approach and defined the local energy dissipated (E_p) in terms of plastic work as an indicator for FCI. Manonukul and Dunne[10] reported that FCI can be accurately modelled by using a very simple crack initiation criterion based on the critical accumulated slip (p_{crit}). In the work by Shenoy et al,[3] 5 fatigue indicator parameters (FIPs) were introduced in order to account for the factors that influence FCI and SCG. These parameters were the accumulated plastic slip per cycle (P_{cyc}), the impingement of slip due to pile-ups (P_r), the critical accumulated plastic slip that leads to crack initiation (p_{crit}), the modified Fatemi-Socie parameter (P_{FS}) that takes into account the tensile stress normal to the crack and the shear strain range acting along the crack, and the maximum range of cyclic shear strain (P_{mps}).[3] Similarly to Shenoy et al, Bozek et al and Hochhalter et al[6-8] used 5 nucleation metrics to model FCI and SCG regimes. These metrics were the maximum accumulated slip over each slip system (nucleation metric D1), the maximum accumulated slip over each slip plane (D2), the maximum accumulated slip over all slip systems (*D3),* the maximum energy dissipated along the critical slip plane (D4), and the modified Fatemi-Socie criterion (D5).[6-8] Table 1 summarizes all the different FIPs used in the above papers.

A general conclusion from all these studies is that various FCI parameters are employed to study the same physical process, ie, FCI, which means that a generic criterion has not yet been derived. Furthermore, the criteria used above have not been verified experimentally down to the microstructural level. This necessitates the development of a coupled in situ micromechanical testing and CPFE modelling approach, such that observations made within individual grains (formation of slip bands and crack nucleation locations) can be compared with the microstructure-informed model prediction.

Micromechanical testing inside a SEM has been successfully applied to a range of alloys extending from high strength steels to titanium and nickel-based superalloys, but most studies have been limited to simple tensile testing.[19-25] A recent study has focused on the effect of cyclic loading on twinning and detwinning in Mg alloys, by combining in situ testing with CPFE modelling.[26] However, that work did not reveal the mechanisms that drive slip band formation, strain localization, and subsequent crack formation.

This work aims at generating new experimental insight into the physical mechanisms that lead to FCI at the microstructural scale in an AA2024 aluminium alloy and to predict experimentally observed FCI locations. Low-cycle fatigue tests are conducted inside a scanning electron microscope (SEM) on bespoke bending specimens coupled with high-resolution imaging to analyze the intragranular deformation mechanisms that lead to crack initiation and early propagation. Electron backscattered diffraction (EBSD) and digital image correlation (DIC) measurements are also conducted to analyze the effect of crystal orientations and local strain fields in the microstructure on FCI. Experimental results are used in combination with CPFE modelling to simulate the cyclic deformation of the microstructure of AA2024 aluminium alloy and to infer a new microstructure-informed FCI criterion.

2 | MATERIALS AND METHODS

AA2024 T3 aluminium alloy was used in this study, received in plate form with 40-mm thickness. At the centre of the plate, the grains were relatively large with an average grain size of approximately 200 μm, while toward the free surface of the plate, the grain size was approximately 50 μm.

Two types of tests were performed for this alloy: macroscopic and microscale. The macroscopic tests consisted of tensile, cyclic fatigue, and fully reversed fatigue using standard geometries. This set of tests was done in order to obtain the macroscopic behaviour of the material and

TABLE 1 Fatigue parameters for indicating damage initiation and small crack growth

K.-S. Cheong, M. J Smillie, and D. M Knowles[18]	$E_p = \int \boldsymbol{\sigma} : \mathbf{L}^{\mathrm{p}} dt, \quad \mathbf{L}^{\mathrm{p}} = \mathbf{F}^{\mathrm{p}} \mathbf{F}^{\mathrm{p}\,-\,1}$
Manonukul and F. Dunne[10]	$p_{\mathrm{cyc}} N_f = p_{\mathrm{crit}}$
M. Shenoy, J. Zhang, and D. L. McDowell[3]	$P_{\mathrm{cyc}} = \int_{\mathrm{cyc}} \sqrt{\frac{2}{3}} \dot{p} \ dt = \int_{\mathrm{cyc}} \sqrt{\frac{2}{3} \mathbf{D}^{\mathrm{p}} : \mathbf{D}^{\mathrm{p}}} dt$ $P_{\mathrm{cyc}} N_{\mathrm{inc}} = p_{\mathrm{crit}}$ $P_r = \max\left(\int_{\mathrm{cycle}} \dot{\varepsilon}^{\mathrm{p}}_{ij} \eta_i t_j \ dt \right)$ $P_{\mathrm{FS}} = \frac{\Delta \gamma^{\mathrm{p}}_{\max}}{2} \left[1 + k^* \frac{\sigma_n^{\max}}{\sigma y} \right] P_{\mathrm{mps}} = \frac{\Delta \gamma^{\mathrm{p}}_{\max}}{2}$
J. D. Hochhalter, D. J. Littlewood, R. J. Christ Jr, M. G. Veilleux, J. E. Bozek, A. M. Maniatty, and A. R. Ingraffea[6-8]	$\gamma^{\alpha} = \int_0^t \lvert \dot{\gamma}^{\alpha} \rvert dt$ $D_1 = \max_{\alpha} \gamma^{\alpha}$ $D_2 = \max_{p} \gamma^{p}$ $D_3 = \gamma = \sum_{\alpha=0}^{Ns} \gamma^{\alpha}$ $D_4 = \max_{p} \int_0^t \sum_{\alpha=0}^{Nd} \left\lvert \dot{\gamma}^{\alpha}_p \tau^{\alpha}_p \right\rvert dt$ $D_5 = \max_{p} \int_0^t \sum_{\alpha=0}^{Nd} \left\lvert \dot{\gamma}^{\alpha}_p \right\rvert \left(1 + k \frac{\langle \sigma^p_n \rangle}{g_o} \right) \ dt$

calibrate the CPFEM material parameters. The strains were measured during testing by (10 mm) strain gauges attached on the surface of the sample. The measurements were also verified by (10 mm) virtual strain gauge measurements made at the back side of the specimens via DIC, DaVIS 7.0 software, LAVision.[27]

Microscale testing was then done within the SEM chamber to study the mechanisms of strong slip band formation and crack nucleation. Bending specimens were machined to a rectangle 50-mm long, 7-mm wide, and 4-mm thick with a 1-mm diameter through-thickness hole drilled at the centre of the specimen to promote the early onset of a fatigue crack. The corresponding geometry is shown in Figure 1A. Four-point cyclic bending was performed ($R = 0$) to evaluate the grains prone to strong slip band formation and fatigue crack nucleation. The results from cyclic bending specimens with a 1-mm machined hole are primarily discussed in this work, as the main focus of this paper is FCI.

For the 2 tests presented in this study, the average grain sizes were 207 and 44 μm at the centre and at the surface of the plate, respectively. The top surface of the sample was then mechanically ground and polished down to 0.06 μm (with Silico solution) followed by electro-polishing in a solution containing 30% nitric acid and 70% methanol, for 13 seconds, at −16°C, 15 V, and 10 mA. Electron back-scattered diffraction measurements were carried out using a FEI-Sirion SEM, at 20 kV, and spot size 5 as operating conditions. The step size was 1.5 and 1.0 μm for the large grained and small grained specimen, covering approximately a total area of 1.6 mm × 3.0 mm and 0.9 mm × 2.3 mm for the 2 samples, respectively. The corresponding EBSD maps are shown in Figure 1B and C. Figure 1D and E shows the inverse pole figures for the EBSD maps of Figure 1B and C, respectively. The texture components for the 2 EBSD maps are similar. The texture in both cases is relatively weak with a maximum intensity of 2.1 times random. A large portion of the inverse pole figure shows orientations in green (about 1 times random), suggesting that a large number of grains are randomly orientated. Some grains, though, show a preferred orientation (red contour), lying along the 001 and 101 boundary.

Following the EBSD measurements, the samples were repolished with Silico solution for 4 minutes, to remove any hydrocarbon deposition generated during the EBSD-measurement acquisition. The samples were then etched with Keller's reagent (95-mL water, 2.5-mL nitric acid, 1.0-mL hydrochloric acid, and 1.5-ml hydrofluoric acid) for approximately 4 to 5 seconds, to reveal the microstructural features such as GBs, particles, and inclusions.

Low-cycle fatigue tests were performed using a 2-kN Deben out-of-plane 4-point bending stage inside a CamScan SEM with a cross head speed of 2 mm/min. The test configuration enables the top surface of the specimen to be under maximum tensile loading, promoting fatigue crack formation on the surface visualized using SEM imaging. Initially, a static test was carried out up to a maximum strain value of 0.01 (for the large-grained sample) and 0.008 (for the small-grained sample), measured

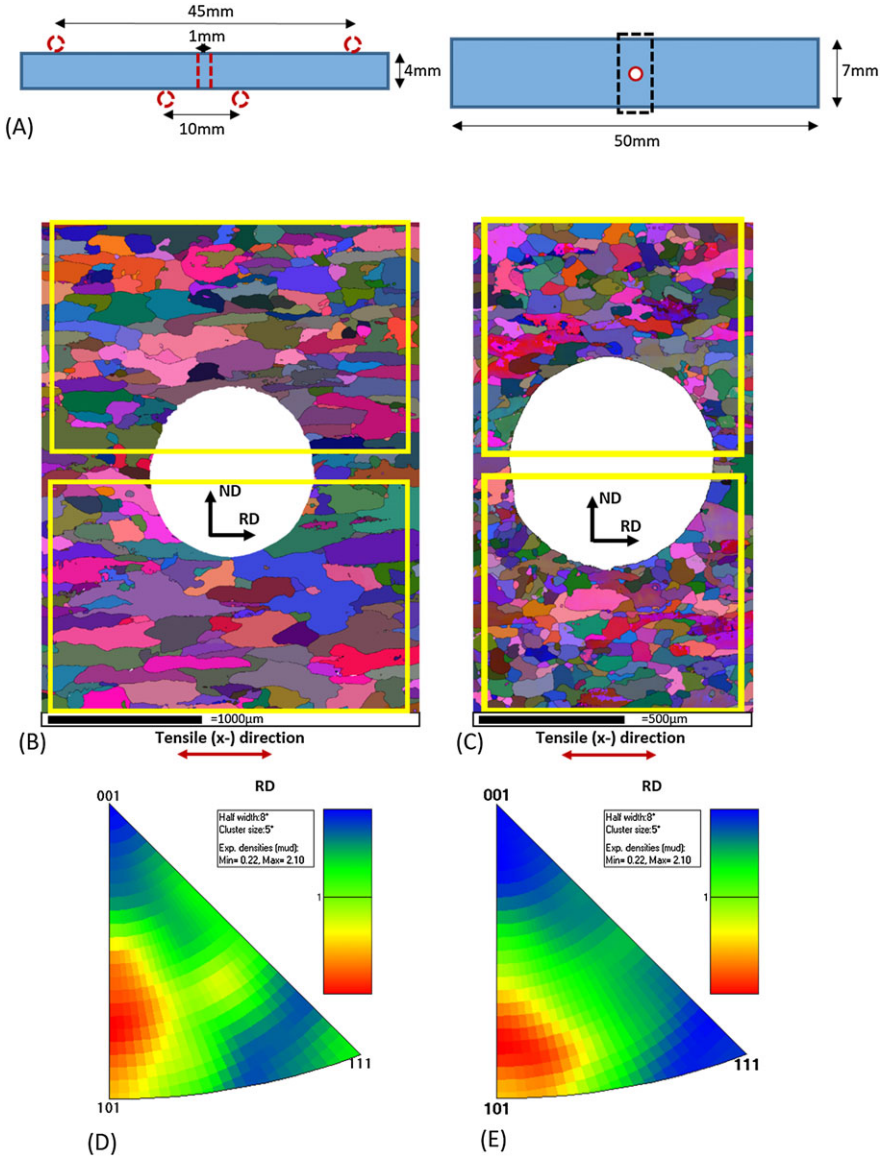

FIGURE 1 (A) Specimen geometry and (B and C) the electron back-scattered diffraction (EBSD) map at the centre of the sample in the region around the hole. The 2 regions of the EBSD map highlighted with yellow boxes were selected for digital image correlation analysis and in situ scanning electron microscope observations during cyclic-bending. D and E, Inverse pole figures for the EBSD map of Figure 1B and C [Colour figure can be viewed at wileyonlinelibrary.com]

using DIC, through displacement values recorded on both left and right edges of the EBSD map shown in Figure 1B and C, respectively. A lower strain amplitude was applied for the small grained sample, as plastic localizations appeared earlier in the test. The test was interrupted every 0.2-mm vertical displacement increments to acquire images. The local displacement and strain values were then measured at the grain scale by means of DIC, using the natural features of the microstructure (precipitates, inclusions, and GBs) for the correlation between 2 successive images, as explained in Ghadbeigi et al.[19] The local strain distributions were first acquired at maximum displacement after static loading (first peak load). Subsequently, displacement controlled cyclic loading was initiated with a frequency of 0.5 Hz, from minimum displacement (zero load) up to maximum displacement. The test was interrupted after the 1st, 10th, 100th, 200th, 300th, 400th, and 500th cycles, at the maximum applied displacement, and images were acquired. All images were correlated with respect to the image at the first peak load and hence to the image of the undeformed sample. Therefore, the total strain values and the plastic strain accumulation were obtained at the scale of the microstructure throughout the whole test. A low magnification was used to acquire images of relatively large microstructural areas with respect to the EBSD map shown in Figure 1B and C, in order to obtain representative results. The 2 regions of the (large-grained) microstructure shown in Figure 1B analyzed with DIC cover approximately a 2.25 mm × 1.5 mm area each and are highlighted with 2 yellow boxes. Similarly, for the small-grained specimen shown in Figure 1C, the regions analyzed with DIC cover approximately a 1.3 mm × 0.8 mm area. The micrographs were analyzed using the commercial DIC software, DaVIS 7.0, LAVision to compute the in-plane displacement field from which the strain values were calculated, as

explained in Ghadbeigi et al.[19] A sensitivity analysis was pursued relative to the interrogation window size. Instead of using a constant interrogation window defined by the number of pixels, a multipass procedure of 4 passes, 2 passes with 32 × 32 pixels, and another 2 with 16 × 16 pixels was selected for all the experimental results presented in this work. This procedure allows for a progressive reduction of the interrogation window, in order to obtain accurate measurements of the strains at the grain level. A 25% overlap between windows has been used to achieve the best correlation results, and a displacement accuracy of 0.01 pixel was obtained, with a strain resolution of about 0.1%. In the following section, results for the 2 analyzed regions of the EBSD maps of Figure 1B and C are presented.

3 | EXPERIMENTAL RESULTS

Four-point cyclic bending was done within the SEM chamber for a set of 6 samples. Cracks formed both at the geometrical edges of the hole but also at the neighbourhood of the machined holes at a distance from the edge of the hole. Figure 2A to D shows a series of SE micrographs for 4 cyclically tested specimens. The formation of fatigue cracks is evident both at the edges of the

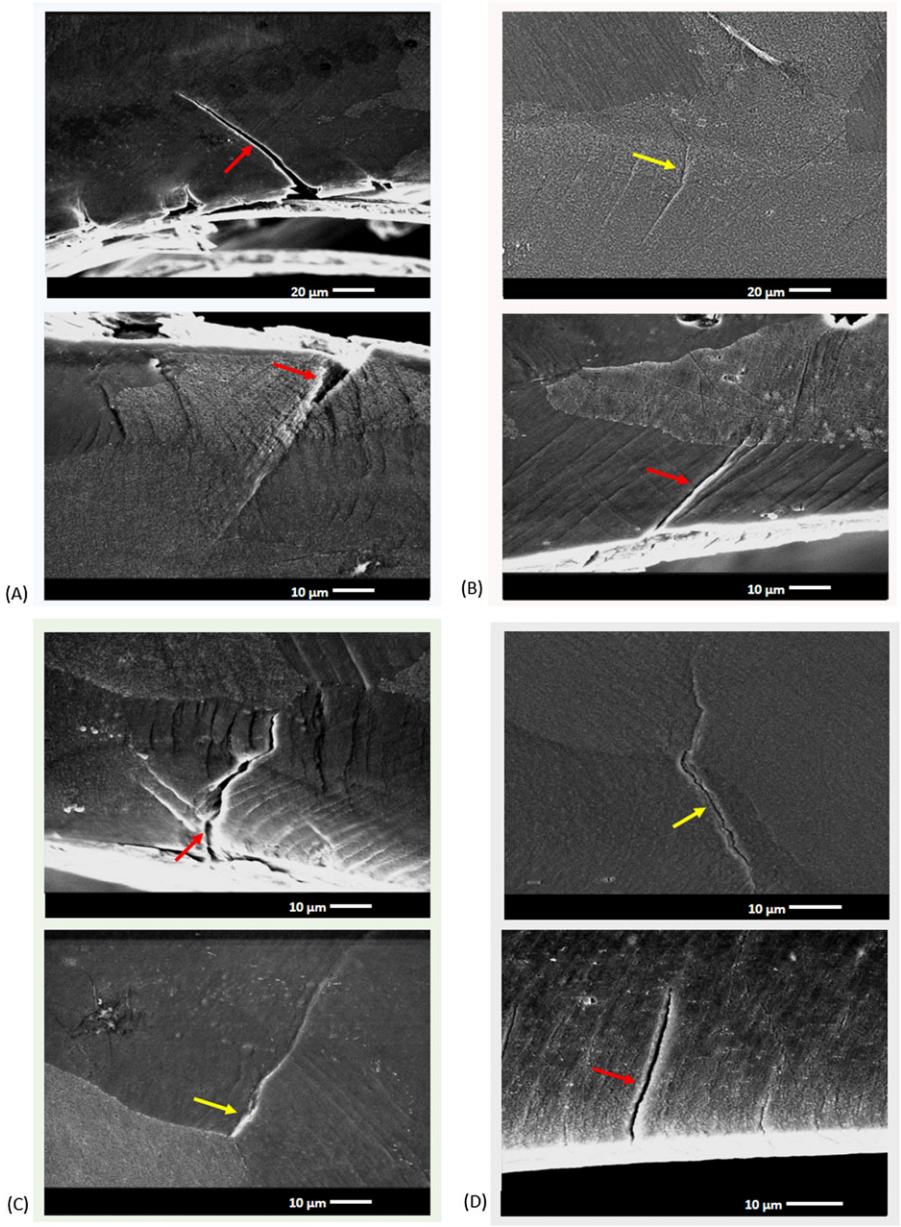

FIGURE 2 Scanning electron micrographs showing the formation of fatigue cracks for 4 specimens tested under cyclic bending. Cracks formed either at the edge of the machined hole (red arrowed locations) or away from the geometric edge of the hole (yellow arrowed locations) [Colour figure can be viewed at wileyonlinelibrary.com]

machined hole as pointed by red arrows and away from the edges as pointed by the yellow arrows. These observations have led to the formulation of this study to further understand the mechanisms that drive crack nucleation either at the edge of the hole or away from it.

3.1 | Local deformation, intense slip band formation, and strain measurements

Scanning electron microscope images recorded during the 4-point bending cyclic tests were used to study microstructure evolution in the 2 regions of the microstructure highlighted by yellow boxes in Figure 1B. Cracks were found to initiate in these 2 regions. After only 10 cycles, intense slip bands can be seen in the grains highlighted in red in Figure 3A and C and in the grain highlighted in white in Figure 3C. It is interesting to note that both grains highlighted in red in Figure 3A and in white in Figure 3C are located close to the hole, but not exactly at the geometrical edge of the hole, therefore suggesting the influence of the microstructure and, in particular, grain orientation on the

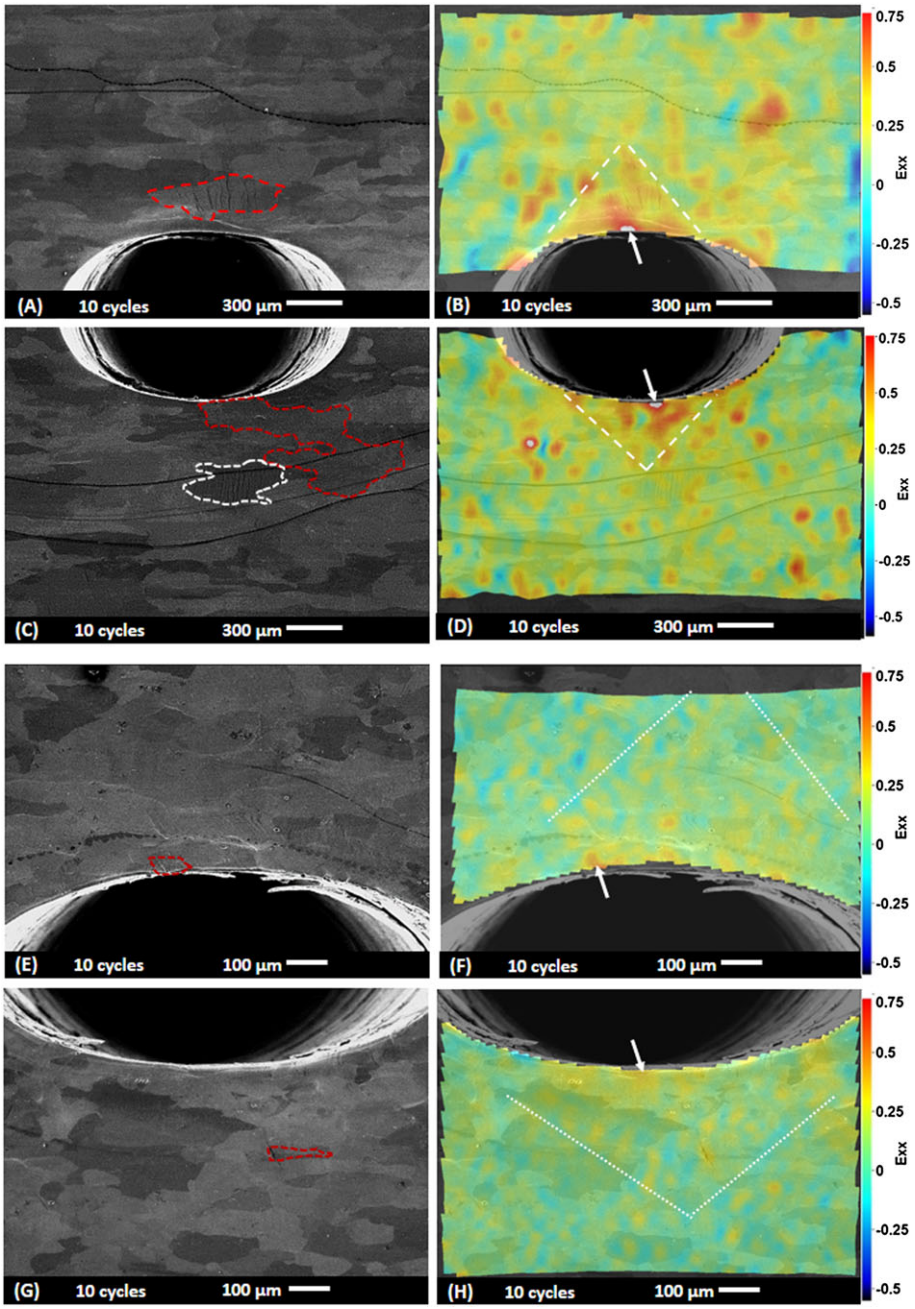

FIGURE 3 A and C and E and G, Scanning electron microscope images of the microstructural areas highlighted in Figure 1B and C, after 10 cycles. B and D and F and H, Corresponding strain maps measured using digital image correlation for the same regions (the *x* axis corresponds to the tensile direction, which is horizontal in these images). [Colour figure can be viewed at wileyonlinelibrary.com]

local plastic deformation during cyclic loading. The DIC-computed ε_{xx} strain (along the tensile axis) distributions in Figure 3B and D show the high heterogeneity of the deformation at the scale of the microstructure. A concentration of high strain values is clearly visible at the edge of the hole (regions highlighted with a white triangle) in Figure 3B and D as expected from the presence of the hole. More localized regions of high strain values are also observed in these strain maps further away from the hole and suggest, again, the influence of grain orientations on local deformation. In the triangular regions of Figure 3B and D, the highest strain magnitude of 0.78 is located at the very edge of the hole as shown by the white arrows in Figure 3B and D. Although such location corresponds to the region of intense slip band formation in the grain highlighted in red in Figure 3C, such correlation is not always observed, as intense slip bands are also observed in the grain highlighted in red in Figure 3A as well as in the grain highlighted in white in Figure 3C, the latter being located outside the triangular region of high strain values.

The results for the small grained sample were similar. After only 10 cycles, intense slip bands can be seen in the grains highlighted in red in Figure 3E and G. One of the grains lies at the very edge of the hole, while the other one is located away from it, similarly to the observations made in Figure 3A and C.

The strain distributions are also very heterogeneous in Figure 3F and H, with the highest strain values of 0.53 measured at the geometrical edge of the hole (locations highlighted with white arrows). However, the locations where the maximum strain values are measured do not always experience intense slip band formation as such bands are not observed at the very edge of the hole in Figure 3G. This result is similar to the observations made in Figure 3a, where the intense slip bands formed away from the edge of the hole, within the red highlighted grain.

3.2 | Fatigue crack initiation

3.2.1 | Crack nucleation along slip bands

Figure 4A and B shows higher magnification SEM images of the grain highlighted in red in Figure 3A, after 1 and 10 cycles, respectively. These close-up views of the microstructure reveal that, although the formation of intense slip bands can actually be observed after the first cycle, FCI can only be clearly seen after 10 cycles along ` of the slip bands in Figure 4B as shown by the red arrow. Figure 4C and D shows high magnification SEM images of the grain highlighted in red in Figure 3C, after 1 and 10 cycles, respectively. Crack initiation does not occur after the first cycle, but microvoids can be seen in the close-up view of Figure 4C as highlighted by the red arrows. Similar observations of microvoid formation along slip bands have been observed by Panin et al.[28] After 10 cycles, these microvoids have joined up to form a crack along a particular slip band, as shown by the red arrow in Figure 4D. These results therefore show that FCI does not always take place at the very edge of the hole where strain magnitudes are the highest but rather in grains favourably orientated for intense slip band formation.

Results are similar for the small grained material. Figure 4E and G shows that strong slip bands formed in the grains highlighted in red in Figure 3E and G. These bands led to the formation of microcracks after 10 cycles as shown by the red arrows in Figure 4F and H.

Fatigue crack initiation requires a certain level of strain intensity to generate a crack as can be seen in Figure 3B and D with a close-up view of the grain highlighted in white in Figure 3C shown in Figure 5. Although intense slip bands can be observed after the first cycle in this grain located about 500-μm away from the hole and outside the triangular region of high strain values in Figure 3D, a crack does not form in this grain, even after 500 cycles (Figure 5B). It is interesting to note that the morphology and density of slip bands in this grain hardly change between 1 and 500 cycles. Fatigue crack initiation in AA2024 T3 is therefore dependent on strain magnitude, grain orientation, and propensity for intense slip band formation, with cracks originating along intense slip bands in highly deformed grains. The ε_{xx} strain values are 0.55 and 0.78 at the location where crack initiation occurs in the 2 grains highlighted in red in Figure 3A and C, respectively. The corresponding strain value in the grain highlighted in white in Figure 3C is 0.4, with no crack formation observed. As for the small-grained material, strain values of 0.53 (at the edge of the hole in Figure 3E) and 0.36 (away from the geometrical edge of the hole in Figure 3G) are measured at crack initiation locations.

4 | COMPUTATIONAL STUDY

4.1 | Constitutive equations

The CPFE model is based on the work of Huang, Hill, and Rice.[29] However, modifications have been made to the original hardening law in order to model cyclic loading conditions. The key equations are reported below with the total deformation gradient F of a crystalline material decomposed into an elastic (F^e) and plastic part (F^p):

$$F = F^e F^p \tag{1}$$

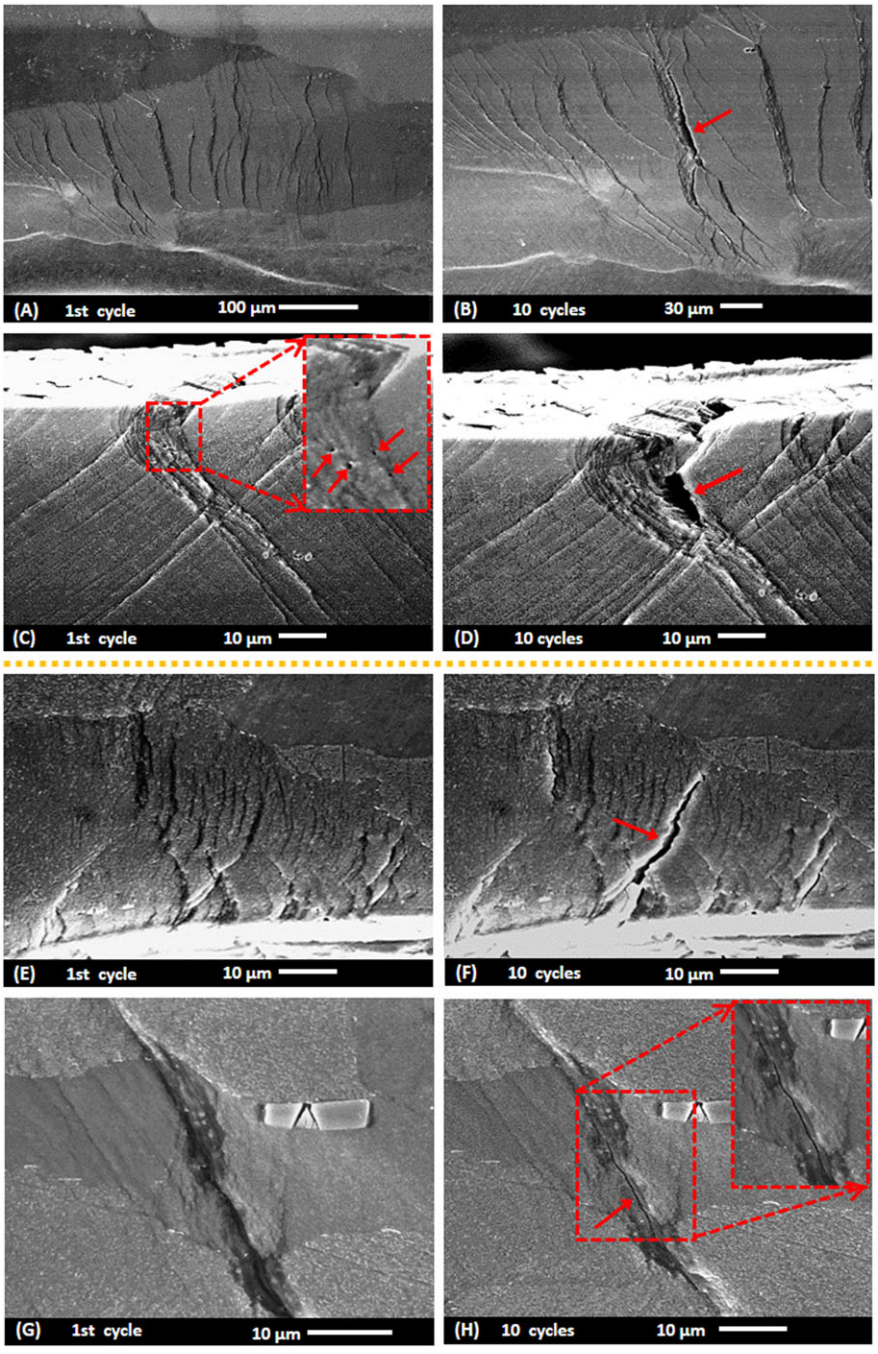

FIGURE 4 Scanning electron microscope images of the grains highlighted in red in Figure 3A and C under tensile loading after 1 cycle (A) and (C) and 10 cycles (B) and (D), respectively. Scanning electron microscope micrographs of the grains highlighted in red in Figure 3E and G under tensile loading after 1 cycle (E) and (G) and 10 cycles (F) and (H), respectively [Colour figure can be viewed at wileyonlinelibrary.com]

$$L = \dot{F} \cdot F^{-1} \tag{2}$$

$$\dot{F} = \dot{F}^{e} \cdot F^{p} + F^{e} \cdot \dot{F}^{p} \tag{3}$$

$$L^{p} = \dot{F}^{p} \cdot F^{p-1} = \sum_{a} \dot{\gamma}^{(a)} \, s^{(a)} \otimes m^{(a)} \tag{4}$$

$$\tau^{(a)} = \sigma : \left(s^{(a)} \otimes m^{(a)} \right)_{sym} \tag{5}$$

where L is the velocity gradient and the dot product is the first derivative with respect to time. The plastic part of the velocity gradient L^{p} and the resolved shear stress $\tau^{(\alpha)}$ are given by

$\dot{\gamma}^{(a)}$ is the slip rate along each slip system α, and s and m are the slip and the normal directions to the slip plane, respectively. σ is the Cauchy stress tensor. The velocity gradient can be decomposed into a symmetric rate of

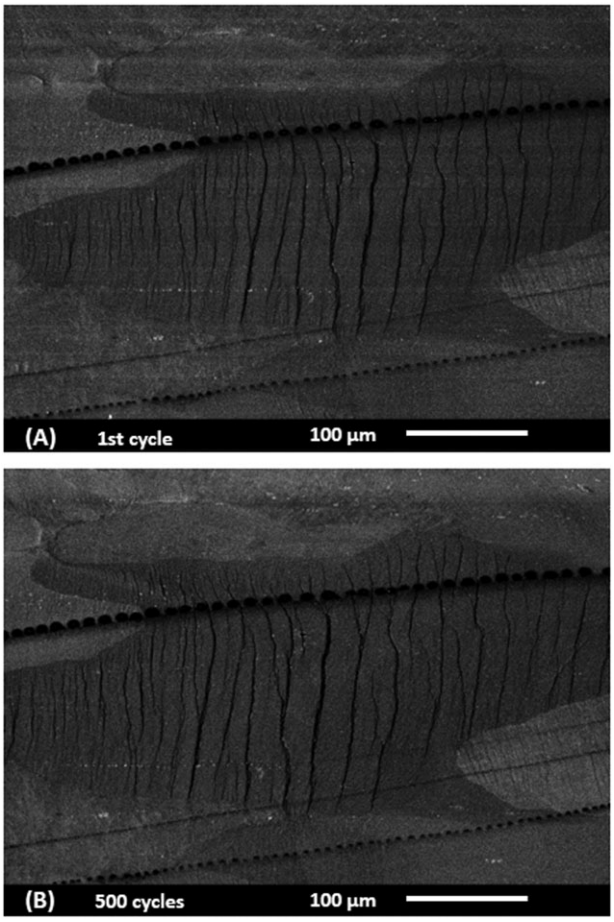

FIGURE 5 Scanning electron microscope images of the grain highlighted in white in Figure 3C under tensile loading after (A) 1 cycle and (B) 500 cycles

stretching tensor D and an antisymmetric spin tensor Ω, while D and Ω can be decomposed into lattice (D^{l}, Ω^{l}) and plastic components (D^{p}, Ω^{p}) as follows:

$$D = D^{\mathrm{l}} + D^{\mathrm{p}} \tag{6}$$

$$\Omega = \Omega^{\mathrm{l}} + \Omega^{\mathrm{p}} \tag{7}$$

with

$$D^{\mathrm{l}} + \Omega^{\mathrm{l}} = \dot{F}^{\mathrm{e}} \cdot \dot{F}^{\mathrm{e}-1} \tag{8}$$

$$D^{\mathrm{p}} + \Omega^{\mathrm{p}} = \sum_{a} \dot{\gamma}^{(\mathrm{a})} s^{(\mathrm{a})} \otimes m^{(\mathrm{a})} \tag{9}$$

The stretching tensor (D) and the Jaumann rate of Cauchy stress, $\widetilde{\sigma}$, are given by[30-32]

$$\widetilde{\sigma} + \sigma(I : D^{\mathrm{e}}) = L : D^{\mathrm{e}} \tag{10}$$

where I is the second-order identity tensor. For monotonic loading conditions, the slip rate, $\dot{\gamma}^{(\mathrm{a})}$ is related to the corresponding resolved shear stress as shown below (Schmid law)[30]:

$$\dot{\gamma}^{(a)} = \dot{\gamma}_0^{(\mathrm{a})} \left| \frac{\tau^{(\mathrm{a})}}{g^{(\mathrm{a})}} \right|^{\mathrm{n}} \mathrm{sign}\left(\tau^{(\mathrm{a})}\right) \tag{11}$$

where $\dot{\gamma}_0^{(\mathrm{a})}$ is the reference strain rate on the αth slip system, n is the strain rate exponent, and $g^{(\alpha)}$ determines the current strength of the αth slip system. For cyclic loading conditions, in order to reflect the contribution of the back-stresses, g^{α} and χ^{α} are introduced to represent the isotropic and kinematic hardening, respectively[31,32]:

$$\dot{\gamma}^{(\mathrm{a})} = \dot{\gamma}_0^{(\mathrm{a})} \left| \frac{\tau^{(\mathrm{a})} - \chi^{(\mathrm{a})}}{g^{(a)}} \right|^{\mathrm{n}} \mathrm{sign}\left(\tau^{(\mathrm{a})} - \chi^{(\mathrm{a})}\right) \tag{12}$$

The hardening law for g^{α} and χ^{α} can be obtained by using the Armstrong-Frederick hardening rule[31-33]:

$$\dot{g}^{(\mathrm{a})} = \sum_{\beta} h_{a\beta} \dot{\gamma}^{(\beta)} \tag{13}$$

$$\dot{\chi}^{(\mathrm{a})} = b\dot{\gamma}^{(\mathrm{a})} - r\chi^{(\mathrm{a})} \left| \dot{\gamma}^{(\mathrm{a})} \right| \tag{14}$$

where the self ($h_{\alpha\alpha}$) and latent ($h_{\alpha\beta}$) hardening moduli are given by

$$h_{aa} = h(\gamma) = h_0 \, \mathrm{sech}^2 \left| \frac{h_0}{\tau_s - \tau_0} \right|, \quad \text{for } a = \beta \tag{15}$$

$$h_{a\beta} = q \, h(\gamma), \quad \text{for } a \neq \beta \tag{16}$$

b, r, and q are material constants; h_o is the initial hardening modulus, τ_s is the stage I critical resolved shear stress, and τ_0 is the saturation critical resolved shear stress, while the cumulative shear strain on all slip systems, γ, can be obtained by

$$\gamma = \sum_{a} \int_0^t \left| \dot{\gamma}^{(a)} \right| dt \tag{17}$$

The above material model was implemented into an Abaqus 6.9 UMAT subroutine,[34] and the geometry and orientation of the individual crystals were created using an Abaqus python scripting interface.

4.2 | Finite element model of the microstructure

For this study, a 2D representative volume element (RVE) was used to predict the macroscopic cyclic stress-strain behaviour from modelling the accumulation of plastic deformation within the individual grains using a CPFE model. Instead of modelling the exact microstructure, the Voronoi technique was employed to create the (2D) microstructure geometry, following principles described in Ghosh, Simonovski and Cizelj, ABAQUS, Roters et al, Simonovski, and Simonovski et al.[4,12,35-38] This was done to create a generic computationally-efficient model[4,35] independent of local geometrical details, such as grain boundaries in the microstructure, which should not affect the overall response of an RVE for the prediction of overall stress/strain curves.

A homogenization study was carried out with a 2D RVE with different number of grains, and it was found that 80 crystals are adequate to efficiently model the macroscopic response for the artificially created microstructure. Grain orientations were assigned to the numerical microstructure by using 3 random number generators for the 3 Euler angles based on the texture of Figure 1 D, through a Fortran subroutine (Intel Visual Fortran version 9.1).[34] A mesh sensitivity study was carried out using 4-node plane strain quadrilateral elements (CPE4). A python code was developed in order to optimize the mesh size (computational time versus homogenized stress-strain fields prediction). Figure 6A and B shows the 2D RVE of 80 Voronoi polygons and the final mesh, respectively. The bottom edge of the polycrystal was gripped in the *y* direction, while the top edge was left free to move, the left-edge was gripped in the *x* direction, and an applied strain of 0.02 was applied at the right edge to match the experimental strain value measured with DIC.

The material parameters (elastic constants and hardening coefficients) for AA2024 aluminium alloy are shown in Table 2 and were obtained from Luo and Chattopadhyay, Luo et al, Simonovski et al, and Asaro.[31-33,39,40] Only h_o, τ_s, and τ_0 parameters were calibrated to obtain the best fit with the macroscopic stress-strain curve. As shown in Figure 7A, a rather good agreement between the experiment and the modelling results was obtained.

In order to model the cyclic behaviour of the material, the values of the parameters *b* and *r* were calibrated using strain-controlled, fully reversed cyclic fatigue tests with

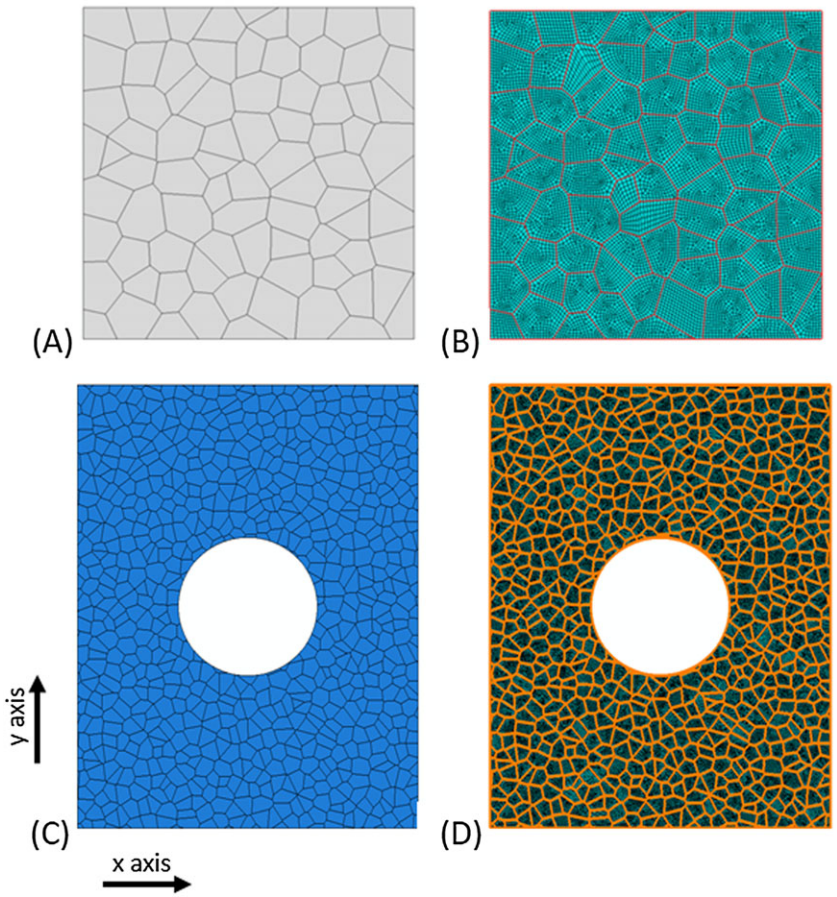

FIGURE 6 (A) The polycrystalline geometry of the 2D representative volume element (RVE) and (B) the meshed microstructure generated to calibrate the material parameters. C, The 2D RVE with the 1-mm machined hole, generated to represent the experimental geometry and (D) the corresponding meshed microstructure [Colour figure can be viewed at wileyonlinelibrary.com]

TABLE 2 Material parameters for AA2024

Elastic Moduli (GPa)							
C_{1111}	C_{1122}	C_{2222}	C_{1133}	C_{2233}	C_{3333}	C_{1112}	C_{2212}
112	59.5	114	59	57.5	114	1.67	−0.574
C_{3312}	C_{1212}	C_{1113}	C_{2213}	C_{3313}	C_{1213}	C_{1313}	C_{1223}
−1.09	26.7	1.25	−0.125	−1.12	−1.92	26.2	−0.125
C_{2223}	C_{3323}	C_{1123}	C_{1323}	C_{2323}			
1.86	0.068	−1.92	−1.09	24.7			
Hardening exponent and hardening coefficient							
$\dot{\gamma}_0$ (s^{-1})				n			
0.001				10			
Self and latent hardening							
h_0 (MPa)	τ_0 (MPa)	τ_s (MPa)		q	b	r	
37	100	82.5		1	−24	1	

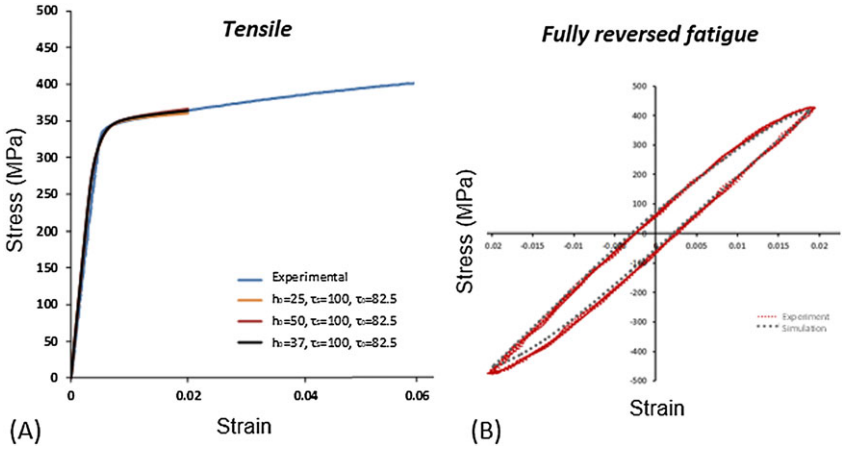

FIGURE 7 Comparison between modelling and experimental results for (C) tensile testing (for a strain up to 0.02) and (D) fully reversed fatigue testing of AA2024 (strain amplitude of 0.02) [Colour figure can be viewed at wileyonlinelibrary.com]

strain amplitude of 0.02. Further details about the procedure to obtain the 2 parameters can be found in Luo and Chattopadhyay and Luo et al.[31-33] Figure 7B shows the good agreement between the curves computed from the CPFE model and the experimentally obtained stabilized curve.

Cyclic loading ($R = 0$) was also applied to the 2D RVE of Figure 6B, to obtain the accumulated shear strain along individual slip systems. Figure 8A shows, as an example, 2 points in neighbouring grains where at one point, Point A, strain accumulation occurs, while at Point B, cyclic softening occurs. Aluminium alloys are FCC crystals and have 12 slip systems that are shown in Table 3. Figure 8B shows the accumulation of plastic strain within the 12 individual slip systems, during the first 10 cycles at point A in Figure 8A. The third slip system is the major slip system accumulating high shear strain plastic slip upon cyclic loading. Apart from the first 3 slip systems (first, second, and third), the other slip systems remain relatively inactive, without any noticed shear strain accumulation.

4.3 | Modelling FCI

Figure 6C and D show the 2D RVE generated in order to simulate the actual experimental geometry with the 1-mm machined hole. Only the large-grained material was simulated as the observations of FCI locations were similar for both the large-grained and small-grained specimens. The total number of grains was approximately 900. In sections 2 and 3, the experimental EBSD map contained 787 grains in a rectangular area of 4.8 mm^2. A larger number of grains were used in the simulation, as the shape of the grains was not accounted for. The grains in Figure 1B are elongated due to the rolling process, while in the model, the grains have a polygonal, rather equiaxed shape as shown in Figure 6C and D.

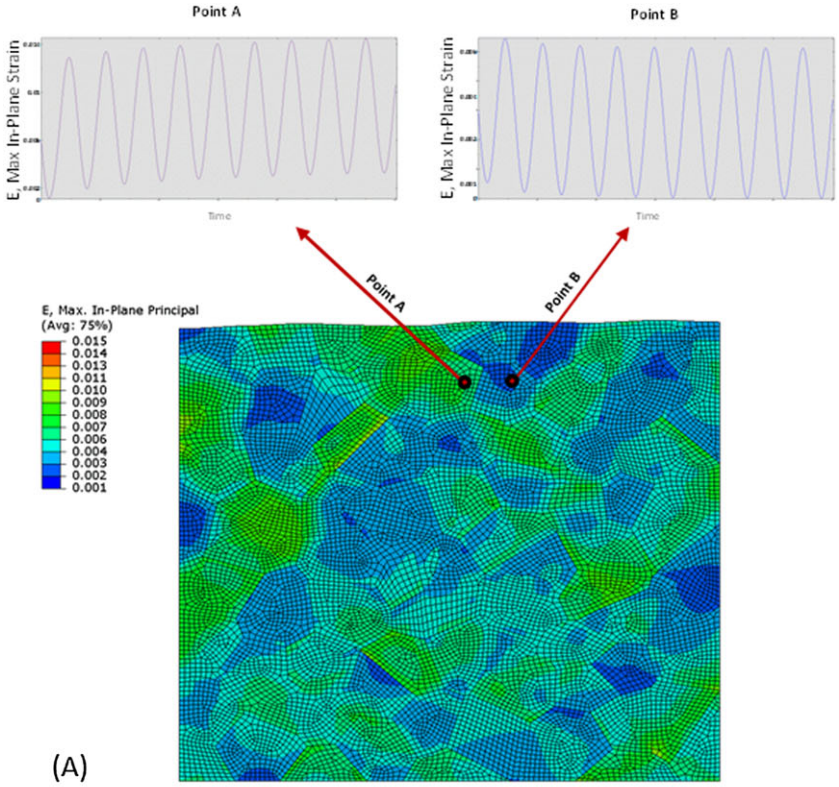

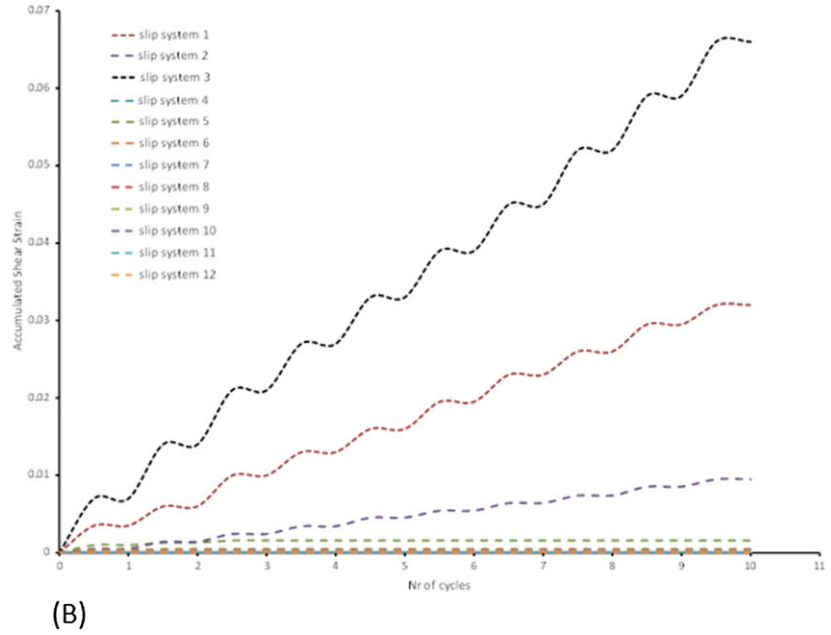

FIGURE 8 A, Maximum in plane strain deformation for the representative volume element of Figure 8A, under cyclic loading conditions, at maximum displacement and after 10 cycles. The 2 points show the corresponding hardening and softening that occurs at the highlighted points A and B. B, Accumulated shear strain for each slip system against the number of cycles at location A in Figure 8A [Colour figure can be viewed at wileyonlinelibrary.com]

The experimentally measured grain diameter along the direction perpendicular to the loading direction, and which corresponds to the crack propagation direction, was selected to calculate the grain size for the equiaxed grains in the simulation. The grain orientations were again random numbers selected from the sets of Euler angles obtained from the EBSD map of Figure 1B. A tensile strain of 1% was applied to the right edge to match the experimental value measured with DIC, with the bottom and left sides being clamped in the y and x directions, respectively.

Following the concepts presented in Table 1, and based on the observations made in sections 3.1 and 4.2, a new FIP parameter is introduced in this work, namely, D^*. Using the notation introduced by Bozek et al and Hochhalter et al[6-8] the D1 metric was selected, which represents the maximum accumulated slip over each slip system, to take into account the effect of crystallographic

TABLE 3 Slip systems in aluminium polycrystals

Number	Slip Plane	Slip Direction
1	(1 1 1)	[0–1 1]
2	(1 1 1)	[1 0–1]
3	(1 1 1)	[−1 1 0]
4	(−1 1 1)	[1 0 1]
5	(−1 1 1)	[1 1 0]
6	(−1 1 1)	[0–1 1]
7	(1–1 1)	[0 1 1]
8	(1–1 1)	[1 1 0]
9	(1–1 1)	[1 0–1]
10	(1 1–1)	[0 1 1]
11	(1 1–1)	[1 0 1]
12	(1 1–1)	[−1 1 0]
Total number of slip systems		12

orientation on FCI, along with the D3 metric, which is the total accumulated slip over all slip systems, representing the effect of strain magnitude on FCI. The new D^* is a combination of the 2 metrics D1 and D3 written as follows:

$$D^* = \sqrt[3]{D1^2 \cdot D3}$$

The $\sqrt[3]{.}$ root is used in order to obtain similar units to those of D1 and D3 metrics. For this study, the exponents for D1 and D3 have values of 2 and 1 in order to reflect the importance of these metrics in relation to experimental observations made in this work. This FIP combines D1 and D3 metrics as it is the presence of critical grains (experiencing strong slip bands) within regions with high strains that lead to FCI. In areas where high strains are observed, cracks initiate preferentially in grains with critical orientations (which facilitate the formation of strong slip bands), and that is the reason why the exponent for the D1 metric is twice that for the D3 metric. The D3 metric is also important, as it was found that critical grains outside the highly deformed regions highlighted with triangles in Figure 3 B and D formed strong slip bands but did not lead eventually to FCI (section 4.2), as the strain values were not high enough to facilitate crack nucleation. This is evident in Figure 5 where intense slip bands form within the first fatigue cycle, but the strain amplitude is not adequate to nucleate a fatigue crack.

Figure 9A shows that the maximum accumulated slip over all slip systems, the D3 metric, after 1 cycle at maximum applied displacement, is highly nonhomogeneous. The highest strain localization occurs at the edge of the hole. The maximum value for D3 is 0.037 at the very edge

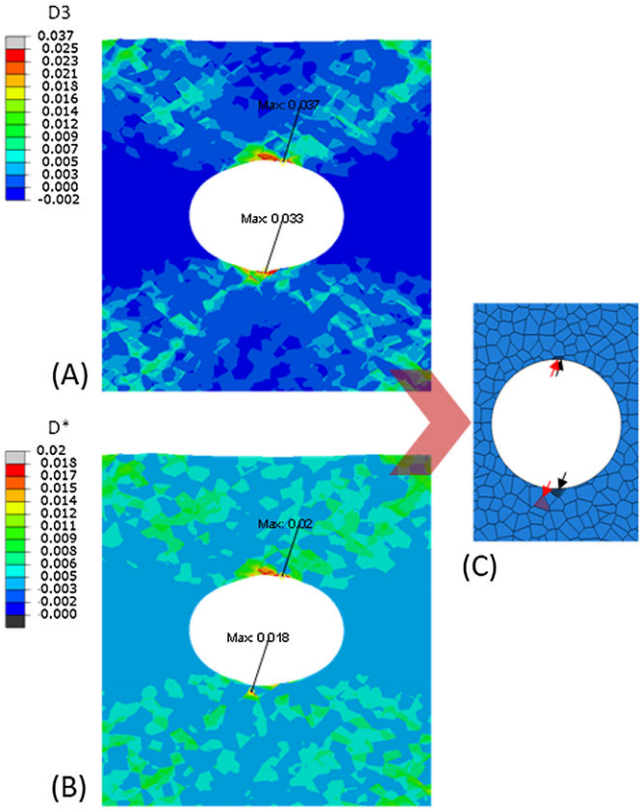

FIGURE 9 (A) D3 and (B) D^* metric distributions after one cycle and (C) predicted location for damage initiation using the D3 (black arrowed locations) and D^* metrics (red arrowed locations) [Colour figure can be viewed at wileyonlinelibrary.com]

of the hole, and therefore, a criterion based on D3 predicts FCI at the edge of the hole. Similar observation can be made on the other side of the hole, with the highest strain value of 0.033 found at the very edge of the hole. Figure 9B shows the distribution of the newly introduced FIP, D^*. The distribution of D^* appears to be even more heterogeneous in comparison with Figure 9 A, showing the increased influence of the individual grains. The highest value for D^* is found to occur at the very edge of the hole, similarly to the strain contours shown in Figure 9A. However, at the other side of the hole, the highest D^* value is predicted to occur at a location away from the edge of the hole. Figure 9C shows more clearly the location of the grains where FCI is predicted using both the D3 and D^* metrics. The grains predicted to initiate a crack by using the D3 metric are shown with black arrows, and both grains are located at the very edge of the hole. By using the newly introduced FIP, D^*, the grains (highlighted with a red arrow) where FCI is predicted to occur are indeed located either at the very edge on one side of the hole and away from the edge on the other side, as observed experimentally. The 2 metrics, D3 and D^*, can therefore lead to very different predictions of the FCI process.

5 | DISCUSSION

5.1 | The effect of local strain distributions on FCI

Figure 3 showed that the strains were highly heterogeneous around the hole. During cyclic loading, strain localization occurred close to the drilled-hole region, as expected due to the stress concentration generated by the hole. However, highly strained regions were found to be next to low strained regions, even within the same grains. A triangle of high strain localization at the edge of the hole was drawn in Figure 3B and D to highlight the main region of strain localization around the hole. Similar triangular regions of high local strains were also observed for the small grained material, as shown in Figure 3F and H. Yet, crack nucleation was found to occur not always at the edge of the hole. Figures 3 and 4 show that slip band formation was the main mechanism that lead to FCI (for high-amplitude loading). A damage-prone grain, close to the edge of the hole in Figures 3A and 4A and B, formed strong slip bands followed by crack formation and propagation along the intense slip bands. Similarly, a damage-prone grain, exactly located at the very edge of the hole in Figures 3C and 4C and D, experienced the formation of strong slip bands at the edge of the hole followed by FCI after only 10 cycles. There was no grain size effects on the FCI mechanisms found in this study by comparing the results on small grained and large grained samples.

The mechanism that leads to crack formation is highlighted in Figure 4C, where small, submicron voids form prior to crack initiation. High magnification imaging revealed that the size of these voids was approximately 0.3 to 0.5 μm. It is the accumulation of high numbers of dislocations along the slip bands that leads to submicron void formation. Once this void density becomes critical, a crack forms, joining together the aligned voids. The appearance of the crack is relatively sudden, with the crack length already reaching 10 μm after 10 cycles. This is due to the presence of these voids, which suddenly join up forming a microcrack (Figure 4D). Fatigue crack initiation is a process involving a large amount of ductility for high-amplitude loading. Large out of plane deformation has occurred at the FCI location with extensive plasticity. This is due to the large driving force that is necessary to initiate a fatigue crack.[2,41]

5.2 | Fatigue indicating parameters

Several FIPs (fatigue indicating parameters) have been suggested in the literature from a modelling point of view.[3,4,6-9,14] Most frequently, the maximum accumulated slip over all the slip systems, the maximum accumulated slip over each slip system, and a local Fatemi-Socie parameter have been used to describe both fatigue initiation and SCG regimes. Yet, there is no published work suggesting which parameter can correctly describe the exact location where FCI occurs in the microstructure of a polycrystal.

One important observation made in this study is that the DIC-measured strain value is not always an adequate parameter or indicator for the exact location where crack initiation occurs. Figure 3 showed that the maximum DIC-measured strain occurred at the very edge of the hole. Yet, the specific grain experiencing that maximum strain value showed uniform plastic deformation without the formation of any strong slip bands. Therefore, the location where the highest strains occurred did not necessarily lead to the formation of intense slip bands (and consequently to crack formation). Instead, a "weak" grain within (the triangle of) the highly strained region forms strong slip bands in Figures 3A and 4A leading to FCI. In contrast, the presence of a "weak" grain in Figures 3C and 4C localizes the highest strains in the form of slip bands exactly at the very edge of the hole. In this case, the location of the highest DIC-measured strain value coincides with the location where crack nucleation occurs. Therefore, in this particular case, the maximum accumulated strain can be an indicator for crack nucleation. However, such indicator would not be able to predict FCI in grains located away from the edge of the hole. Similar observations were made in Figure 3E to H. Crack nucleation does not always occur at the very edge of the hole where the highest strains are measured. Similarly, the maximum accumulated slip over each slip system is not an adequate FIP parameter either. A "weak" grain in Figure 5 is located away from the highly deformed triangular region, and while strong slip bands form just after the first cycle, the local stress-strain conditions do not facilitate crack formation. It is therefore suggested in this work that an alternative FIP needs to be introduced to reproduce experimental results. This new FIP incorporates both the effect of total plastic strain (measured using DIC) through the total accumulated slip over all slip systems (D3 metric) and the effect of critical grain orientations through the D1 metric or maximum accumulated slip over each slip system (plasticity along critical slip systems). This results from the fact that it is the presence of critical grains, in critical regions (of highly localized strains) that lead to FCI. Therefore, it is the combination of the 2 FIPs, D1 and D3, that can correctly and geometrically predict FCI. Figure 9 shows that the newly introduced FIP, D^*

metric, which is the multiplication of D1 and D3 metrics, predicts damage nucleation both at the edge of the hole and in the region near the edge of the hole, in accordance with the experimental observations for all tests carried out in this study.

More experiments are necessary in the future to validate the importance and the relative effect of the 2 parameters, namely, D1 and D3. There could also be an influence of the material investigated on the values of the 2 exponents. Different polycrystals, such as nickel superalloys, Ti alloys, or steels, might yield different dependence between the 2 metrics. The effect of specimen geometry, including different notches, on results could also be studied although the conditions for FCI are not expected to change. As far as sample thickness is concerned, because the microstructure and especially grain orientations play a significant role on FCI, it is probably the grain size to sample thickness ratio that needs to be considered. Results from this work have shown that for the same specimen thickness and a different grain size, and for a similar nearly random texture, FCI indeed occurred in a similar way. This criterion is also valid for crack nucleation along strong slip bands and for identifying the critical grains. For microcracking at second-phase particles, concepts and modelling procedures such as those outlined in the work of Bozek et al and Hochhalter et al[6-8] should be considered. However, even for the case of low amplitude high cycle fatigue, for which cracks nucleate at particle sites, the local stress-strain fields within individual grains greatly influence crack nucleation and propagation.

6 | CONCLUSIONS

A new experimental procedure combining 4-point cyclic out-of-plane bending in a SEM on a specimen with a 1-mm-diameter machined hole and full-field strain and orientation measurements has enabled new insights into FCI and SCG mechanisms in AA2024. Digital image correlation measurements carried out during cyclic loading showed high strain values concentrated in triangular regions adjacent to the hole. Results obtained on several specimens showed that cracks did not always initiate at the edge of the hole where the highest strains were measured but rather in critical grain of particular orientations within the highly strained regions around the hole. Based on these experimental observations, a new FCI criterion, D^*, was thus proposed, which combines 2 parameters: the maximum accumulated slip over all slip systems that accounts for the maximum plastic strain and the accumulated slip along the critical slip system that accounts for the orientation effect that leads to the formation of strong slip bands. A 2D Voronoi-based CPFEM was developed to simulate the fatigue tests at the scale of the microstructure. It was found that by using the maximum accumulated slip as a FCI criterion, damage is always predicted to occur at the edge of the hole due to the high strain concentration. Instead, by using the modified FCI criterion, D^*, results show that damage may initiate at a distance away from the hole depending on the presence of a critical grain orientation. The effect of the microstructure can therefore be accounted for by using the newly introduced criterion, and a more accurate prediction of the location of FCI can be obtained for this alloy. Results provide useful insights for designing crystalline materials with superior fatigue performance and address the necessity of coupling in situ testing with microstructural modelling in order to obtain accurate models for the FCI regime.

ACKNOWLEDGEMENT

The authors are grateful for the financial support provided by the Engineering and Physical Sciences Research Council in the UK under the grant EP/F023464/1 to carry out this work.

Abbreviations

2D	two-dimensional
CPFE	crystal plasticity finite element
DIC	digital image correlation
EBSD	electron back-scattered diffraction
FCI	fatigue crack initiation
FE	finite element (modelling)
FIPs	fatigue indicator parameters
GB	grain boundary
RVE	representative volume element
SCG	small crack growth
SEM	scanning electron microscope
T3	type of temper used in aluminium alloys
UMAT	user material (subroutine)

NOMENCLATURE

Literature Review

E_p	local energy dissipation
p_{crit}	critical accumulated slip
P_{cyc}	accumulated slip per cycle
P_r	cumulative net plastic shear strain

P_{FS}	local Fatemi-Socie parameter that accounts for both the accumulated shear strain along the crack and the tensile stress normal to the crack
P_{mps}	maximum range of cyclic plastic shear strain
D1, D2, D3, D4, and D5	the maximum accumulated slip over each slip system, over each slip plane, over all slip systems, the maximum energy dissipated along the critical slip plane, modified Fatemi-Socie criterion that accounts for the tensile stress normal to the crack, and the shear strain range acting along the crack, respectively
L_p	plastic component of the velocity gradient
$\dot{F}^p$	plastic deformation gradient
N_f	number of cycles to failure
D^p	plastic component of D
N_{inc}	number of cycles to initiate a crack
t and n	the directions along a given slip plane and the normal to that plane
k^*	material properties related to multiaxial strain state
$\Delta\gamma^p_{max}$	maximum range of plastic shear strain,
σ_n^{max}	peak tensile stress normal to the slip plane
σ_y	cyclic yield strength
γ^a, $\dot{\gamma}^a$	slip and slip rate along each slip system α
γ	cumulative shear strain on all slip systems
γ^p,$\dot{\gamma}^p$	plastic slip and plastic slip rate
k	parameter dictating the importance of tensile stress relative to plastic slip
$\langle\sigma_n^p\rangle$	tensile stress on slip plane p
$\langle \ldots \rangle$	Macaulay brackets; $\langle x\rangle = 0$ if $x \leq 0$ and $\langle x\rangle = x$ if $x > 0$
N_d	total number of slip systems on a given slip plane
g_0	the initial hardness (resistance to slip) on the slip systems

This work

R	ratio between minimum and maximum peak stress
ε_{xx}	major strains along the horizontal tensile axis
F, F^e, F^p	total deformation gradient, elastic deformation gradient
L:	velocity gradient
$\dot{F}$, $\dot{F}^e$	rate of change of the deformation gradient, elastic, and plastic deformation gradient; respectively
$\tau^{(\alpha)}$, σ	resolved shear stress and Cauchy stress tensor
D, Ω	symmetric rate of stretching tensor of the velocity gradient L, antisymmetric spin tensor of the velocity gradient L
D^l, Ω^l	lattice components of D and Ω
D^p, Ω^p	plastic components of D and Ω
$\widetilde{\sigma}$	Jaumann rate of Cauchy stress
I	second-order identity tensor
D^e	elastic component of D
$\dot{\gamma}_{0^{(\alpha)}}$ and $g^{(\alpha)}$	reference strain rate and current strength on the α^{th} slip system as given by Schmid law
g^α and χ^α	represent the isotropic and kinematic hardening in Frederik-Armstrong rule
$\dot{\varepsilon}^p$	plastic shear strain rate along a specific slip system
γ^α	accumulated slip for slip system α
τ^p_α	resolved shear stress over slip system α
b, r, and q	material constants
h_o	initial hardening modulus
τ_s	stage I critical resolved shear stress
τ_0	critical resolved shear stress at saturation
CPE4	4-node plane strain quadrilateral element
D^*	FIP parameter which combines the 2 metrics D1 and D3

ORCID

Panos Efthymiadis http://orcid.org/0000-0002-5733-0145

REFERENCES

1. Suresh S. Fatigue of Materials. In:1998.
2. Miller KJ. Metal fatigue—past, current and future. *Proc Inst Mech Eng C J Mech Eng Sci*. 1991;205(5):291-304.
3. Shenoy M, Zhang J, McDowell DL. Estimating fatigue sensitivity to polycrystalline Ni-base superalloy microstructures using a computational approach. *Fatigue Fract Eng Mater Struct*. 2007;30(10):889-904.

4. Ghosh S. *Micromechanical Analysis and Multi-Scale Modeling Using the Voronoi Cell Finite Element Method*. Taylor & Francis: CRC Press; 2011.
5. McDowell DL, Dunne FPE. Microstructure-sensitive computational modeling of fatigue crack formation. *Int J Fatigue*. 2010;32(9):1521-1542.
6. Bozek JE, Hochhalter JD, Veilleux MG, et al. A geometric approach to modeling microstructurally small fatigue crack formation: I. In: Probabilistic simulation of constituent particle cracking in AA 7075-T651, Modelling and Simulation in Materials Science and Engineering 16(6).2008:065007.
7. Hochhalter JD, Littlewood DJ Jr, RJC, et al. A geometric approach to modeling microstructurally small fatigue crack formation: II. Physically based modeling of microstructure-dependent slip localization and actuation of the crack nucleation mechanism in AA 7075-T651. *Model Simul Mater Sci Eng*. 2010;18(4):045004.
8. Hochhalter JD, Littlewood DJ, Veilleux MG, et al. A geometric approach to modeling microstructurally small fatigue crack formation: III. Development of a semi-empirical model for nucleation. *Model Simul Mater Sci Eng*. 2011;19(3):035008.
9. Dunne FPE, Rugg D, Walker A. Length scale-dependent, elastically anisotropic, physically-based hcp crystal plasticity: application to cold-dwell fatigue in Ti alloys. *Int J Plast*. 2007;23(6):1061-1083.
10. Manonukul A, Dunne FPE. High- and low-cycle fatigue crack initiation using polycrystal plasticity. *Proc R Soc London Ser A: Math, Phys Eng Sci*. 2004;460(2047):1881-1903.
11. Priddy MW, Paulson NH, Kalidindi SR, McDowell DL. Strategies for rapid parametric assessment of microstructure-sensitive fatigue for HCP polycrystals. *Int J Fatigue*. 2017;104:231-242.
12. Simonovski K-FN I, Cizelj L. Material properties calibration for 316L steel using polycrystalline model. In: *ICONE 13: Proceedings of the 13th International Conference on Nuclear Engineering Beijing*; 2005.
13. Chen B, Jiang J, Dunne FPE. Microstructurally-sensitive fatigue crack nucleation in Ni-based single and oligo crystals. *J Mech Phys Solids*. 2017;106:15-33.
14. Guan Y, Chen B, Zou J, Britton TB, Jiang J, Dunne FPE. Crystal plasticity modelling and HR-DIC measurement of slip activation and strain localization in single and oligo-crystal Ni alloys under fatigue. *Int J Plast*. 2017;88:70-88.
15. Przybyla CP, McDowell DL. Microstructure-sensitive extreme value probabilities for high cycle fatigue of Ni-base superalloy IN100. *Int J Plast*. 2010;26(3):372-394.
16. McEvily AJ. The growth of short fatigue cracks: a review. *Mater Sci Res Int*. 1998;4(1):3-11.
17. Brinckmann S, Van der Giessen E. A fatigue crack initiation model incorporating discrete dislocation plasticity and surface roughness. *Int J Fract*. 2007;148(2):155-167.
18. Cheong KS, Smillie MJ, Knowles DM. Predicting fatigue crack initiation through image-based micromechanical modeling. *Acta Mater*. 2007;55(5):1757-1768.
19. Ghadbeigi H, Pinna C, Celotto S. Quantitative strain analysis of the large deformation at the scale of microstructure: comparison between digital image correlation and microgrid techniques. *Exp Mech*. 2012;52(9):1483-1492.
20. Ghadbeigi H, Pinna C, Celotto S, Yates JR. Local plastic strain evolution in a high strength dual-phase steel. *Mater Sci Eng A*. 2010;527(18–19):5026-5032.
21. Gioacchino FD, da Fonseca JQ. An experimental study of the polycrystalline plasticity of austenitic stainless steel. *Int J Plast*. 2015;74:92-109.
22. Jin H, Lu WY, Korellis J. Micro-scale deformation measurement using the digital image correlation technique and scanning electron microscope imaging. *J Strain Anal Eng Des*. 2008;43(8):719-728.
23. Ososkov Y, Wilkinson DS, Jain M, Simpson T. In-situ measurement of local strain partitioning in a commercial dual-phase steel. *Int J Mater Res*. 2007;98(8):664-673.
24. Tasan CC, Hoefnagels JPM, Diehl M, Yan D, Roters F, Raabe D. Strain localization and damage in dual phase steels investigated by coupled in-situ deformation experiments and crystal plasticity simulations. *Int J Plast*. 2014;63:198-210.
25. Tasan CC, Hoefnagels JPM, Geers MGD. Microstructural banding effects clarified through micrographic digital image correlation. *Scr Mater*. 2010;62(11):835-838.
26. Hazeli K, Askari H, Cuadra J, et al. Microstructure-sensitive investigation of magnesium alloy fatigue. *Int J Plast*. 2015;68:55-76.
27. DaVis Strain Master Software LAVision LTD; 2005.
28. Panin VE, Moiseenko DD, Maksimov PV, Panin SV. Effects of plastic distortion in the lattice curvature zone of a crack tip. *Phys Mesomech*. 2017;20(3):280-290.
29. Huang Y. "A user-material subroutine incorporating single crystal plasticity in the ABAQUS finite element program, Mech report 178". Division of Engineering and Applied Sciences, Harvard University, Cambridge, Massachusetts.
30. Huang Y. A user-material subroutine incorporating single crystal plasticity in the ABAQUS finite element program. In: *Mech Report 178*. Cambridge, Massachusetts.
31. Luo C, Chattopadhyay A. Prediction of fatigue crack initial stage based on a multiscale damage criterion. *Int J Fatigue*. 2011;33(3):403-413.
32. Luo C, Wei J, Parra-Garcia M, Chattopadhyay A, Peralta P. Fatigue damage prediction in metallic materials based on multiscale modeling. *AIAA Journal*. 2009;47(11):2567-2576.
33. Luo C. Multiscale modeling & virtual sensing for structural health monitoring 2011; http://hdl.handle.net/2286/7ozpxe85egh.
34. ABAQUS, Version 6.9. Hibbitt Karlsson and Sorensen, Inc., Providence, RI; 2009.
35. Roters F, Eisenlohr P, Hantcherli L, Tjahjanto DD, Bieler TR, Raabe D. Overview of constitutive laws, kinematics, homogenization and multiscale methods in crystal plasticity finite-element modeling: theory, experiments, applications. *Acta Mater*. 2010;58(4):1152-1211.

36. Simonovski I. Mechanisms for thermal fatigue initiation and crack propagation in NPP components: final report. In: *S.l.: s. n*; 2005.

37. Simonovski I, Nilsson K-F, Cizelj L. Crack tip displacements of microstructurally small cracks in 316L steel and their dependence on crystallographic orientations of grains. *Fatigue Fract Eng Mater Struct*. 2007;30(6):463-478.

38. Simonovski I, Nilsson K-F, Cizelj L. The influence of crystallographic orientation on crack tip displacements of microstructurally small, kinked crack crossing the grain boundary. *Comput Mater Sci*. 2007;39(4):817-828.

39. Asaro RJ. Crystal plasticity. *J Appl Mech*. 1983;50(4b):921-934.

40. Asaro RJ, Rice JR. Strain localization in ductile single crystals. *J Mech Phys Solids*. 1977;25(5):309-338.

41. Miller KJ. The two thresholds of fatigue behaviour. *Fatigue Fract Eng Mater Struct*. 1993;16(9):931-939.

How to cite this article: Efthymiadis P, Pinna C, Yates JR. Fatigue crack initiation in AA2024: A coupled micromechanical testing and crystal plasticity study. *Fatigue Fract Eng Mater Struct*. 2018;1–18. https://doi.org/10.1111/ffe.12909